Astronomy
&
Astrophysics

First extragalactic detection of a phosphorus-bearing molecule with ALCHEMI: Phosphorus nitride (PN)

D. Haasler[1,2], V. M. Rivilla[2,3], S. Martín[4,5], J. Holdship[6,7], S. Viti[6,7], N. Harada[8,9,10], J. Mangum[11], K. Sakamoto[9], S. Muller[12], K. Tanaka[13], Y. Yoshimura[14], K. Nakanishi[8,10], L. Colzi[2,3], L. Hunt[3], K. L. Emig[11,⋆], R. Aladro[15], P. Humire[15], C. Henkel[15,16,17], and P. van der Werf[6]

[1] Escuela Superior de Ciencias Experimentales y Tecnología (ESCET), Universidad Rey Juan Carlos, Tulipán s/n, 28933 Móstoles, Madrid, Spain
e-mail: davidhaaslergarcia@gmail.com
[2] Centro de Astrobiología (CSIC-INTA), Ctra. de Ajalvir Km. 4, Torrejón de Ardoz 28850, Madrid, Spain
[3] INAF – Osservatorio Astrofisico di Arcetri, Largo Enrico Fermi 5, 50125 Florence, Italy
[4] European Southern Observatory, Alonso de Córdova, 3107, Vitacura, Santiago 763-0355, Chile
[5] Joint ALMA Observatory, Alonso de Córdova, 3107, Vitacura, Santiago 763-0355, Chile
[6] Leiden Observatory, Leiden University, PO Box 9513, 2300 RA Leiden, The Netherlands
[7] Department of Physics and Astronomy, University College London, Gower Street, London WC1E6BT, UK
[8] National Astronomical Observatory of Japan, 2-21-1 Osawa, Mitaka, Tokyo 181-8588, Japan
[9] Institute of Astronomy and Astrophysics, Academia Sinica, 11F of AS/NTU Astronomy-Mathematics Building, No.1, Sec. 4, Roosevelt Rd, Taipei 10617, Taiwan
[10] Department of Astronomy, School of Science, The Graduate University for Advanced Studies (SOKENDAI), 2-21-1 Osawa, Mitaka, Tokyo 181-1855, Japan
[11] National Radio Astronomy Observatory, 520 Edgemont Road, Charlottesville, VA 22903-2475, USA
[12] Department of Space, Earth and Environment, Chalmers University of Technology, Onsala Space Observatory, 43992 Onsala, Sweden
[13] Department of Physics, Faculty of Science and Technology, Keio University, 3-14-1 Hiyoshi, Yokohama, Kanagawa 223–8522, Japan
[14] Institute of Astronomy, Graduate School of Science, The University of Tokyo, 2-21-1 Osawa, Mitaka, Tokyo 181-0015, Japan
[15] Max-Planck-Institut für Radioastronomie, Auf dem Hügel 69, 53121 Bonn, Germany
[16] Astron. Dept., Faculty of Science, King Abdulaziz University, PO Box 80203, Jeddah 21589, Saudi Arabia
[17] Xinjiang Astronomical Observatory, Chinese Academy of Sciences, Urumqi 830011, PR China

ABSTRACT

Context. Phosphorus (P) is a crucial element for life given its central role in several biomolecules. P-bearing molecules have been discovered in different regions of the Milky Way, but not yet towards an extragalactic environment.
Aims. We searched for P-bearing molecules outside the Milky Way towards the nearby starburst Galaxy NGC 253.
Methods. Using observations from the ALMA Comprehensive High-resolution Extragalactic Molecular Inventory (ALCHEMI) project, we used the MAdrid Data CUBe Analysis package to model the emission of P-bearing molecules assuming local thermodynamic equilibrium (LTE) conditions. We also performed a non-LTE analysis using SpectralRadex.
Results. We report the detection of a P-bearing molecule, phosphorus nitride (PN), for the first time in an extragalactic environment, towards two giant molecular clouds (GMCs) of NGC 253. The LTE analysis yields total PN beam-averaged column densities $N = (1.20 \pm 0.09) \times 10^{13}\,\mathrm{cm}^{-2}$ and $N = (6.5 \pm 1.6) \times 10^{12}\,\mathrm{cm}^{-2}$, which translate into abundances with respect to H_2 of $\chi = (8.0 \pm 1.0) \times 10^{-12}$ and $\chi = (4.4 \pm 1.2) \times 10^{-12}$. We derived a low excitation temperature of $T_{\mathrm{ex}} = (4.4 \pm 1.3)\,\mathrm{K}$ towards the GMC with the brightest PN emission, which indicates that PN is sub-thermally excited. The non-LTE analysis results in column densities consistent with the LTE values. We also searched for other P-bearing molecules (PO, PH_3, CP, and CCP), and upper limits were derived. The derived PO/PN ratios are <1.3 and <1.7. The abundance ratio between PN and the shock-tracer SiO derived towards NGC 253 follows the same trend previously found in Galactic sources.
Conclusions. Comparison of the observations with chemical models indicates that the derived molecular abundances of PN in NGC 253 can be explained by shock-driven chemistry followed by cosmic-ray-driven photochemistry.

Key words. astrochemistry – galaxies: individual: NGC 253 – ISM: clouds – ISM: molecules – ISM: abundances

1. Introduction

Phosphorus (P), along with oxygen, hydrogen, carbon, nitrogen, and sulfur, is one of the six biogenic elements and it is

essential for the development of life. It has a pivotal role in key biomolecules such as phospholipids that conform the structure of cellular membranes, nucleic acids (e.g. DNA and RNA), or adenosine triphosphate (ATP), which is the molecular energy currency in cells (Maciá 2019). Although P is not abundant in the Universe, it has a vital importance in biology on Earth. Its

---

⋆ Jansky Fellow of the National Radio Astronomy Observatory.

cosmic abundance compared to hydrogen (H) is $\sim 2.6 \times 10^{-7}$ (Asplund et al. 2009), being only the nineteenth most abundant element. For this reason, the detection of P-bearing molecules in the interstellar medium (ISM) is challenging, and as a consequence its interstellar chemistry is still not fully understood. While it is known that P is synthesised in the interior of massive stars (Koo et al. 2013) and injected into the ISM through supernova explosions, it is still a matter of debate how it is incorporated into molecules in molecular clouds (e.g. Rivilla et al. 2020).

To date, several P-bearing molecules have been found in the ISM of our Galaxy, starting with the first simultaneous phosphorus nitride (PN) detections towards massive star-forming regions simultaneously by Turner & Bally (1987) and Ziurys (1987). Afterwards, PN was also detected towards protostellar shocks (Yamaguchi et al. 2011; Lefloch et al. 2016), Galactic Centre molecular clouds (Rivilla et al. 2018), envelopes of evolved stars (Milam et al. 2008; Ziurys et al. 2018), multiple massive star-forming regions (Fontani et al. 2016, 2019; Mininni et al. 2018; Rivilla et al. 2020; Bernal et al. 2021), and the surrounding environment of low-mass protostars (Bergner et al. 2019).

The first detection of interstellar phosphorus oxide (PO) was reported by Tenenbaum et al. (2007) in the circumstellar region of the evolved star VY Canis Majoris. Later, PO was also detected in several massive star-forming regions (Rivilla et al. 2016, 2020; Bernal et al. 2021), a protostellar shock (Lefloch et al. 2016), a Galactic Centre molecular cloud (Rivilla et al. 2018), and a low-mass star-forming region (Bergner et al. 2019). Moreover, PO has also been detected in the coma of the comet Churyumov-Gerasimenko recently thanks to in situ measurements by the Rosetta spacecraft (Rivilla et al. 2020). In all these different environments, it has been found that the molecular abundance PO/PN ratio is always higher than 1.

Other P-bearing molecules have also been detected in our Galaxy, but only in the circumstellar envelopes of evolved stars and/or planetary atmospheres. Phosphine (PH_3) was detected towards IRC+10216 (Agúndez et al. 2014) and in the atmosphere of the gaseous planets Saturn (Bregman et al. 1975) and Jupiter (Larson et al. 1977). In addition CP, CCP, and HCP have also been detected in the envelope of evolved stars (Agúndez et al. 2007, 2014; Halfen et al. 2008; Milam et al. 2008).

So far, all of the detections of P-bearing molecules have been reported in regions of our Galaxy. Although atomic P has been detected towards extragalactic environments, for example in the Large Magellanic Cloud (LMC; Friedman et al. 2000) and in a damped-Lyman absorber towards the quasar QSO 0000-2620 (Molaro et al. 2001), P-bearing molecules outside our Galaxy still have yet to be found. The improved sensitivity of current radiotelescopes (e.g. the Atacama Large Millimeter/sub-millimeter Array, ALMA) allows us to search for P-bearing species beyond our Galaxy. We present in this work a search for P-bearing molecules towards the galaxy NGC 253 using the spectral line survey of the ALMA Comprehensive High-resolution Extragalactic Molecular Inventory (ALCHEMI; Martín et al. 2021). NGC 253 is a nearly edge-on barred spiral galaxy and a prototype of nearby starburst (distance of 3.5 Mpc; Rekola et al. 2005). Its star formation rate of 2 $M_\odot$ yr^{-1} within its central kiloparsec is roughly twice that within the entire Milky Way (Robitaille & Whitney 2010; Leroy et al. 2015; Bendo et al. 2015). The metallicity of NGC 253 is consistent with or just above Solar ($12 + \log(O/H) = 8.99 \pm 0.31$; Marble et al. 2010). The central molecular zone (CMZ) of

NGC 253 is one of the most prolific extragalactic sources for detections of molecules, as shown by previous spectral surveys, which revealed a rich chemical composition (e.g. Martín et al. 2006, 2021; Aladro et al. 2015; Meier et al. 2015; Ando et al. 2017). This fact makes NGC 253 an excellent target for the search of new molecular species in the extragalactic ISM.

2. Observations

We used observations from the ALMA Comprehensive High-resolution Extragalactic Molecular Inventory (ALCHEMI), which is an ALMA Large Program to study the molecular inventory of the starburst Galaxy NGC 253 (Martín et al. 2021). The observations target the CMZ of NGC 253 covering a rectangular area of $50'' \times 20''$, that is 850×340 pc centred at RA(ICRS) = $00^h47^m33.26^s$, Dec(ICRS) = $-25°17'17.7''$. ALCHEMI is an unbiased spectral survey that uses the ALMA main array and ACA (ALMA Compact Array) configurations to fully cover the bands 3, 4, 5, 6, and 7 (from 84.2 to 373.2 GHz) down to an average sensitivity of ~ 15 mK in 10 km s^{-1} channels at a common angular resolution of 1.6$''$ (28 pc). More details about the observations and the data reduction of ALCHEMI are extensively presented in Martín et al. (2021).

3. Data analysis and results

We used MADCUBA[1] (Martín et al. 2019) for the inspection of the ALCHEMI datacubes, the identification of the molecular species, and the LTE derivation of the physical parameters of the emission. The Spectral Line Identification and Modelling (SLIM) tool of MADCUBA generates a simulated spectrum assuming local thermodynamic equilibrium (LTE) conditions. The AUTOFIT tool performs a non-linear least-squares fitting of the simulated LTE spectrum to the observed data utilising the Levenberg-Marquardt algorithm (Levenberg 1944; Marquardt 1963) and provides the best solution for the model parameters: total molecular column density (N), excitation temperature (T_{ex}), line velocity (v_{LSR}), line full width at half maximum (FWHM), and source size (θ_s). Table 1 lists the different molecular transitions analysed in this work, their frequencies, upper energy levels, and Einstein A_{ul} coefficients.

3.1. Detections of phosphorus nitride (PN) and LTE analysis

Using the datacube visualisation tool of MADCUBA, we inspected the CMZ of NGC 253 to search for PN emission towards the Giant Molecular Clouds (GMCs) shown in Fig. 1 (we have adopted the labelling from Leroy et al. 2015), with the exception of GMC 5. This region is located at the position of the dynamical centre of NGC 253 determined by Müller-Sánchez et al. (2010). This region contains several bright (thermal) radio continuum sources that are parsecs in size (Ulvestad & Antonucci 1997; Mills et al. 2021); when this region is observed at $\sim 1''$ resolution, molecular components of the CMZ appear in absorption (Mangum et al. 2019). Because this results in complex spectral line profiles from a variety of molecular species, we do not analyse GMC 5. We used the PN spectroscopic data provided by the Cologne Database

---

[1] MADCUBA (Madrid Data Cube Analysis) is a software developed in Centro de Astrobiología (INTA-CSIC, Madrid) to visualise and analyse single spectra and datacubes.
https://cab.inta-csic.es/madcuba/.

Table 1. Molecular transitions used in the analysis.

Molecule	Transition	Frequency (GHz)	$E_{\rm up}$ (K)	$A_{\rm ul}$ ($\times 10^{-5}$ s^{-1})
PN	$J = 2-1$	93.979	6.8	2.9
	$J = 3-2$	140.967	13.5	10.5
PO [a]	$F = 3-2, l = e$	108.998	8.4	2.1
	$F = 2-1, l = e$	109.045	8.4	1.9
PH$_3$	$J = 1-0$	266.945	12.8	2.4
CP [b]	$F = 3-2$	95.710	6.9	0.4
	$F = 2-1$	95.713	6.9	0.4
CCP [c]	$F = 8-7, l = e$	95.406	19.2	5.3
	$F = 7-6, l = e$	95.410	19.3	5.2
	$F = 8-7, l = f$	95.456	19.3	5.3
	$F = 7-6, l = f$	95.460	19.3	5.3
^{29}SiO	$J = 2-1$	85.759	6.2	2.8
	$J = 3-2$	128.637	12.3	10.2
	$J = 4-3$	171.512	20.6	25.1
C^{34}S	$J = 2-1$	96.412	6.2	1.6
	$J = 3-2$	144.617	11.8	5.8

Notes. [a]$J = 5/2-3/2$, $\Omega = 1/2$. The other two lines of this quadruplet at 109.206 and 109.281 GHz are not used due to heavy contamination from other molecular species. [b]$J = 5/2-3/2$. [c]$J = 15/2-13/2$. $\Omega = 1/2$ Spectroscopic data obtained from the CDMS catalogue: PN entry 045511 (September 2019), PO entry 047507 (October 2019), PH$_3$ entry 034501 (May 2013), CP entry 043501 (March 2000), CCP entry 055503 (April 2009), ^{29}SiO entry 045504 (January 2014), and C^{34}S entry 046501 (January 2004).

for Molecular Spectroscopy (CDMS) catalogue[2] (Müller et al. 2001; Endres et al. 2016) entry 045511 (version of September 2019) based on the works by Cazzoli et al. (2006) and the dipole moment from Hoeft et al. (1972).

We successfully detected PN towards GMCs 4 and 6. The side panels in Fig. 1 present the integrated emission maps of PN(2−1) towards these two molecular clouds. The PN(2−1) transition is not contaminated by other species, as seen in Galactic star-forming regions (e.g. Fontani et al. 2016, 2019; Rivilla et al. 2020) and in Galactic Centre molecular clouds (Rivilla et al. 2018). The emission is enhanced towards the continuum peaks in both GMCs. In GMC 6 it exhibits a tail-like structure towards the south-east at a 2σ level. This emission might be a real feature, but the current sensitivity does not allow us to draw a firm conclusion.

To perform the molecular analysis, we extracted the spectra towards the pixel of the peak of the continuum emission of the GMCs. The spectra of the PN(2−1) transition towards GMCs 6 and 4 are displayed in the left panels of Fig. 2. The transition is detected at levels of 16σ and 5σ in integrated intensity for GMCs 6 and 4, respectively. The right panels of Fig. 2 show the spectra of the PN(3−2) transition, which is detected in GMC 6 and not detected in GMC 4.

Transitions of PN up to the 7−6 fall also within the ALCHEMI spectral coverage, but their expected intensities, according to the fit obtained with the PN(2−1) and PN(3−2) transitions (see below), are <0.6 mJy, below the noise level of the data. Moreover, some PN transitions appear heavily contaminated by transitions of more abundant species: PN(4−3) is contaminated by CH$_3$C$_2$H(11−10) and PN(6−5) by several transitions of HC$_3$N.

To derive the physical parameters of the emission, we used the MADCUBA-AUTOFIT tool. We fixed the source size to $\theta_{\rm s}$ = 1.6″, which matches the ALCHEMI synthesised beam, and hence the derived molecular column densities are beam-averaged. We note that if the PN emission would be confined to the 0.6″ core sizes measured at higher resolution (clumps 1 and 6 in Ando et al. 2017), column densities in this work would be underestimated by a factor of ∼7. Since the uncertainty in the filling factor cancels when comparing species, assuming co-spatial distribution, the column density ratios between species still provide reliable constraints. We also fixed the FWHM to the linewidth that reproduces well the PN(2−1) profiles, which is 50 km s^{-1}. For GMC 6, we left free the other parameters (N, $T_{\rm ex}$, and $v_{\rm LSR}$) while simultaneously fitting the PN(2−1) and PN(3−2) transitions. The resulting best LTE fit is shown with a red curve in the upper panels of Fig. 2 and the derived parameters are listed in Table 2. We obtain a total PN column density $N = (1.20 \pm 0.09) \times 10^{13}$ cm^{-2} and excitation temperature $T_{\rm ex}$ = 4.4 ± 1.3 K. Higher values of $T_{\rm ex}$ (e.g. 10 and 15 K) would result in higher intensities of the PN(3−2) transition, which are not consistent with the observations, as shown in Fig. 2. The low $T_{\rm ex}$ derived is similar to the ones derived in Galactic Centre molecular clouds (Rivilla et al. 2018) and to high-mass and low-mass star forming regions (Fontani et al. 2019; Bergner et al. 2019). Such a low $T_{\rm ex}$ suggests that the molecule is sub-thermally excited. We derived the relative abundance of PN compared to H$_2$, using the total column density of H$_2$, $N_{\rm H_2}$, derived by Mangum et al. (2019) from dust continuum observations with a similar spatial resolution than ALCHEMI (1.5″ × 0.9″). Assuming that PN and dust trace similar volumes of gas (we discuss this assumption in Sect. 4), we obtain an abundance of $\chi = (0.8 \pm 0.1) \times 10^{-11}$ (see Table 2).

For GMC 4, since the PN(3−2) is within the noise level (Fig. 2), we performed the LTE fit using only the PN(2−1) transition and fixing $T_{\rm ex}$ to the one derived in GMC 6. We obtain a total PN column density of $N = (6.5 \pm 1.6) \times 10^{12}$ cm^{-2}, which translates into a PN abundance of $\chi = (0.44 \pm 0.12) \times 10^{-11}$. The results of the fit for GMC 4 are presented in Table 2.

PN is not detected towards the rest of the GMCs, and therefore we provide upper limits for its column density in these regions. MADCUBA calculates the upper limit of the column density using the 3σ value of the integrated intensity (see details in Martín et al. 2019). We fixed $T_{\rm ex}$ and FWHM to the same values as the ones derived in the PN detection of GMC 6, and $v_{\rm LSR}$ to a representative value of each GMC. Table A.1 lists the parameters used for the measurement of the upper limits for each GMC without PN detection. Figures A.3–A.9 show the calculated upper limits for the PN column density in these regions as well.
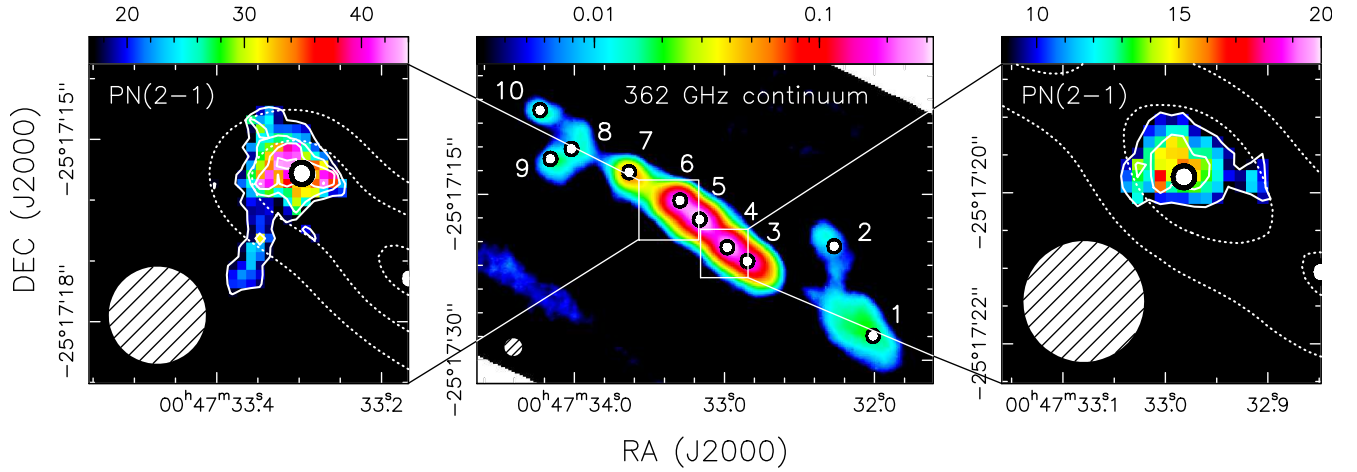
3.2. Non-LTE analysis of PN

We also performed a non-LTE analysis in GMC 6 using SpectralRadex[3] (Holdship et al. 2021). SpectralRadex uses RADEX (van der Tak et al. 2007) to calculate spectral line excitation and optical depth within the large velocity gradient approximation. A Gaussian spectral line profile is assumed to produce model spectra. We used the collisional data between PN and p-H$_2$ (Najar et al. 2017) taken from BASECOL (Dubernet et al. 2013; Ba et al. 2020) and prepared for RADEX with SPECTCOL[4].

---

[2] https://cdms.astro.uni-koeln.de/classic/catalog

[3] https://spectralradex.readthedocs.io
[4] http://www.vamdc.org/activities/research/software/spectcol/

Fig. 1. *Centre*: continuum map of the CMZ of NGC 253 at 362 GHz with a coloured scale indicating the emission in Jy beam^{-1}. The numbered circles represent the brightest points of each GMC detected by Leroy et al. (2015). The synthesised beam of the observations (1.6″) is shown in the lower left corner of each panel with a white hatched circle. *Left*: zoomed in view towards GMC 6 of the integrated emission between 120 and 240 km s^{-1}. *Right*: zoomed in view towards GMC 4 of the integrated emission between 220 and 260 km s^{-1}. Figures on the sides have their integrated emission scale in mJy beam^{-1} km s^{-1} starting at 2σ. The white dashed contour levels indicate the continuum emission for 0.1, 0.2, and 0.3 Jy beam^{-1}. Solid white contours indicate 2σ, 3σ, 4σ and 5σ levels of the PN detection.
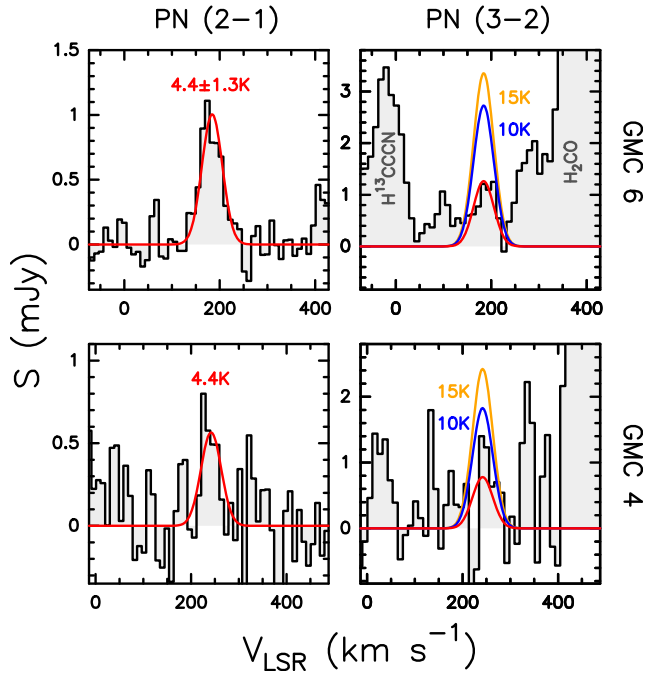
Fig. 2. PN(2−1) (*left*) and PN(3-2) (*right*) transitions towards the GMCs 6 (*upper panels*) and 4 (*lower panels*) of NGC 253. The spectra have been extracted towards the peak of the continuum. The best LTE fits to the line emission are indicated in red. In blue and yellow we show the expected line profiles for PN(3−2) assuming T_{ex} of 10 and 15 K, respectively.

Since SpectralRadex works with intensities in units of K, we converted the intensities using Eq. (3.31) in the ALMA Cycle 8 technical Handbook[5]:

$$T(K) = 13.6 \left(\frac{300\,\text{GHz}}{\nu}\right)^2 \frac{1}{\theta_{max}('') \, \theta_{min}('')} I(\text{Jy beam}^{-1}) \quad (1)$$

[5] https://almascience.nrao.edu/documents-and-tools/cycle8/alma-technical-handbook/view

Table 2. Physical parameters derived for the emission from the molecules analysed in this work towards GMCs 6 and 4 of NGC 253.

Mol.	$N \times 10^{13}$ (cm^{-2})	T_{ex} (K)	v_{LSR} (km s^{-1})	$FWHM$ (km s^{-1})	χ ($\times 10^{-11}$) [a]
			GMC 6		
PN	1.20 ± 0.17	4.4 ± 1.3	184 ± 6	50 [b]	0.80 ± 0.19
PO	<1.5	4.4 [b]	184.2 [b]	50 [b]	<1.0
PH$_3$	<3.2	4.4 [b]	184.2 [b]	50 [b]	<2.2
CP	<3.0	4.4 [b]	184.2 [b]	50 [b]	<2.0
CCP	<3.8	4.4 [b]	184.2 [b]	50 [b]	<2.6
^{29}SiO	9.2 ± 1.8	5.2 ± 0.3	187.4 ± 2.0	70.4 [b]	6.3 ± 1.9
C^{34}S	57 ± 7	6.83 ± 0.21	188.1 ± 0.4	67.8 ± 1.0	39 ± 9
			GMC 4		
PN	0.65 ± 0.17	4.4 [b]	242 [b]	50 [b]	0.44 ± 0.17
PO	<1.1	4.4 [b]	242 [b]	50 [b]	<0.7
PH$_3$	<3.4	4.4 [b]	242 [b]	50 [b]	<2.3
CP	<2.7	4.4 [b]	242 [b]	50 [b]	<1.8
CCP	<2.8	4.4 [b]	242 [b]	50 [b]	<1.9
^{29}SiO	6.1 ± 1.0	5.20 ± 0.23	246.4 ± 1.8	74 ± 4	4.1 ± 1.2
C^{34}S	25 ± 3	7.9 ± 0.5	237.7 ± 1.0	74.4 ± 2.3	17 ± 5

Notes. [a] N_{H_2} taken from Mangum et al. (2019). [b] Parameter fixed.

where T is the brightness temperature, I is the intensity, and θ_{min} and θ_{max} are the axes of the synthesised beam. This allows us to model the spectra as a function of the PN column density, gas temperature and density. We combine this model with emcee (Foreman-Mackey et al. 2013) to perform a Markov chain Monte Carlo (MCMC) sampling of the likelihood. We assume the uncertainty on each channel is independent from the other channels, Gaussian, and 15% of the channel value. The FWHM and v_{LSR} of the lines are taken from Table 2.

The marginalised and joint probability distributions of these parameters are shown in Fig. 3. We find that the gas temperature is poorly constrained, showing a range for T_K between ~50 K to ~300 K. Previous measurements (Mangum et al. 2013, 2019) obtained kinetic temperatures between 50 K and >150 K on size scales as large as 5″ in GMC 6. On smaller scales (~1″) T_K could be as high as 300 K. The most likely value of the column density of PN is 5×10^{12} cm^{-2}. To estimate the uncertainty on this value, we take the region around this most likely value which
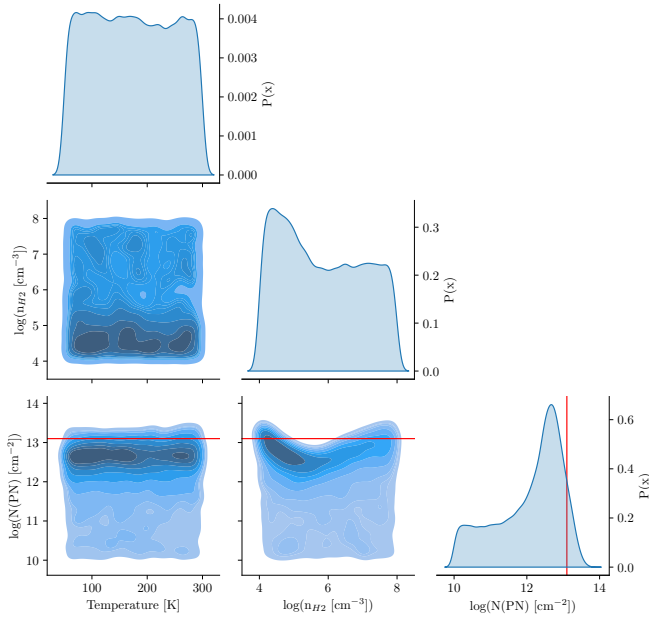
Fig. 3. Marginalised and joint posterior distributions from the MCMC sampling. The 1D distributions show the probability a parameter takes a given value, marginalised over all possible combinations of the other parameters. The 2D distributions are darker where a parameter combination is more likely. Column density, volume density and probability scales are logarithmic. The red lines indicate the value of the PN column density obtained with the LTE analysis.

contains 67% of the probability density (similar to a 1σ interval). This interval is 6.3×10^{11} cm^{-2} to 1.8×10^{13} cm^{-2}. The non-LTE analysis provides us with results that are similar to those seen in the LTE analysis. The LTE value of $N = 1.2 \times 10^{13}$ cm^{-2} (red lines in Fig. 3) falls at the high side of the confidence interval and close to the most likely value of N in the non-LTE analysis (5×10^{12} cm^{-2}).

This non-LTE analysis gives a most likely gas density of 3×10^4 cm^{-3} and the majority of the probability density is at values lower than 10^6 cm^{-3}.

3.3. PO (phosphorus monoxide)

We searched for PO using spectroscopic data from the CDMS catalogue entry 047507 (October 2019) based on the works by Bailleux et al. (2002) and the dipole moment from Kanata et al. (1988) (see Table 1). PO is not detected in any of the GMCs. We show in the left panel of Fig. 4 the spectrum towards GMC 6 (that with the brightest PN detection). This spectral window contains the two PO transitions indicated in Table 1, corresponding to the $J = 5/2-3/2$ $\Omega = 1/2$ quadruplet (the other two lines of this quadruplet are heavily contaminated by other molecular species). We derived an upper limit for PO using the transitions shown in Fig. 4, assuming the FWHM and T_{ex} derived from the LTE analysis of PN. We obtain $N < 1.5 \times 10^{13}$ cm^{-2} for GMC 6 (Table 2), which gives a PO/PN ratio <1.3. The same was made for GMC 4 which results in $N < 1.1 \times 10^{13}$ cm^{-2} and a PO/PN ratio <1.7.

3.4. PH$_3$ (phosphine)

We searched for PH$_3$ using data from CDMS catalogue entry 034501 (May 2013) based on the works by Müller (2013). The

only transition of this species targeted by the ALCHEMI survey is the $1-0$ transition at 266.945 GHz (Table 1). We show in the right panel of Fig. 4 the spectrum at this frequency towards GMC 6. The transition is not detected and we derived an upper limit for the column density. We obtained $N < 3.2 \times 10^{13}$ cm^{-2} (Table 2) for GMC 6, which gives a PH$_3$/PN ratio <2.7. For GMC 4 the results obtained were $N < 3.4 \times 10^{13}$ cm^{-2} and a PH$_3$/PN ratio <5.3.

3.5. Other P-bearing molecules

We also searched for other P-bearing molecules (CP, CCP, HCP, and PS) towards GMCs 4 and 6, where PN is detected. The spectroscopic data of CP, CCP, and HCP was taken from CDMS catalogue entry 043501 (March 2000), entry 055503 (April 2009), and entry 044502 (June 2007), respectively. The spectroscopic data of PS was taken from the entry 63007 (January 1997) of the Jet Propulsion Laboratory (JPL) catalogue[6]. None of these P-bearing species were detected. All of the transitions of HCP and PS are heavily contaminated by other species, which prevents the derivation of significant upper limits for their abundance. For CP and CCP we derived upper limits for their abundances using uncontaminated transitions listed in Table 1. The parameters T_{ex}, v_{LSR}, and FWHM were fixed to the values of the PN detection in each source. The derived upper limits for CP and CCP are $N < 3.0 \times 10^{13}$ cm^{-2} and $N < 3.8 \times 10^{13}$ cm^{-2}, respectively for GMC 6, and $N < 2.7 \times 10^{13}$ cm^{-2} and $N < 2.8 \times 10^{13}$ cm^{-2}, respectively for GMC 4 (Table 2).

### 3.6. Detections of ^{29}SiO and C^{34}S

We also analysed the emission of C^{34}S and ^{29}SiO, an optically-thin isotopologue of SiO, which will be used in the discussion below (Sect. 4). The LTE fits were done with MADCUBA-AUTOFIT, using the same procedure described in Sect. 3.1. The molecular transitions used in the analysis are listed in Table 1. The results of the fits are shown in Figs. A.1–A.9, and Table A.1 lists the derived parameters of the detections.

4. Discussion: phosphorus chemistry

4.1. Correlation between PN and SiO abundances: role of shocks

Although the chemistry of P in the ISM is still poorly constrained, the observations of P-bearing species in the last years have suggested the likely importance of shocks. In Galactic sources (Galactic Centre molecular clouds, massive star-forming regions, and protostellar shocks in the Galactic disk), a good correlation has been established between the abundances of SiO − a well known shock tracer − and those of PN (Rivilla et al. 2018). Following this work, we show in Fig. 5 the column densities of PN and ^{29}SiO, both normalised by the column density of C^{34}S, towards different Galactic sources detected previously. Rivilla et al. (2018) used C^{34}S to normalise the abundances because this optically-thin species is expected to be a good proxy of H$_2$, and it is barely affected by the presence of shocks or photo-dominated regions (Requena-Torres et al. 2006; Martín et al. 2009). We include in Fig. 5 the two points corresponding to the PN detections in GMCs 4 and 6, and the upper limits derived for the rest of the GMCs. The points of

---

6 https://spec.jpl.nasa.gov
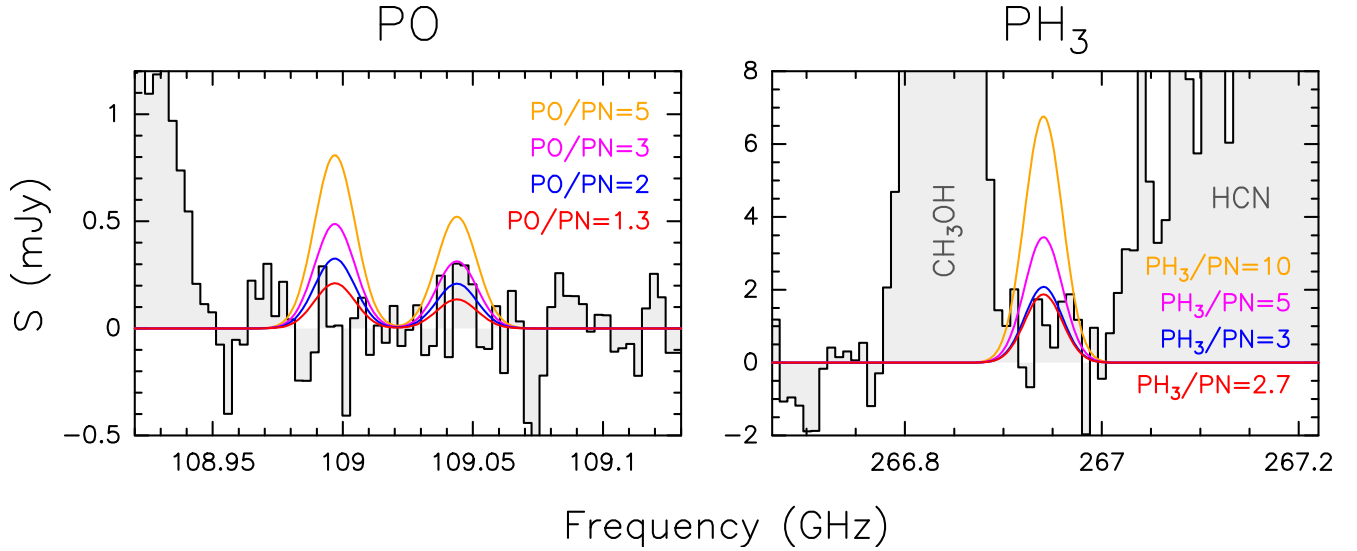
Fig. 4. *Left*: spectrum towards GMC 6 containing the two PO transitions indicated in Table 1. The coloured curves show LTE synthetic models assuming different PO/PN ratios, using the N and the T_{ex} obtained for PN. The red curve corresponds to the calculated upper limit for PO. *Right*: same as in left panel, but for PH$_3$ (1–0).
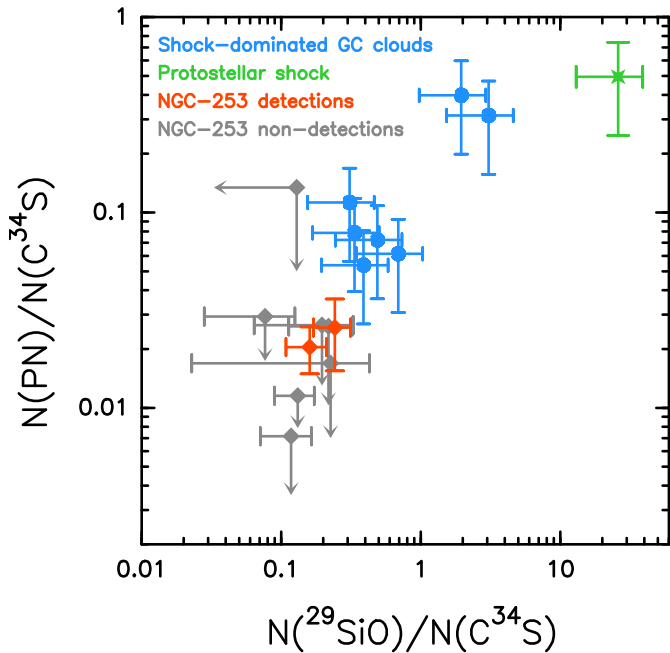
Fig. 5. PN and ^{29}SiO column density ratios relative to C^{34}S. The two detections of PN in NGC 253 (GMCs 4 and 6) are indicated with red diamonds, while the non-detections towards the remaining GMCs are indicated with grey diamonds. We also added data from other sources in our Galaxy Centre (Rivilla et al. 2018 and references therein): in green we plot the L1157-B1 shock data and the blue dots represent data from shock dominated Galactic Centre clouds.

NGC 253 nicely follow the same trend observed in Galactic sources, extending it to lower relative abundances.

This observational evidence suggests that the chemistry of P in extragalactic environments is overall similar to that in our Galaxy. The emission of P-bearing molecules is enhanced in shocked regions, where shock-induced sputtering of grains injects the P locked on the grain surfaces into the gas phase (Rivilla et al. 2020). The main carrier of P on the icy mantles has been suggested to be PH$_3$, which can be rapidly formed by

hydrogenation of atomic P, and that can be converted to PN and PO in the gas phase (see Jiménez-Serra et al. 2018). We note that the only interferometric maps of P-bearing emission available so far, obtained towards the star-forming region AFGL 5142 (Rivilla et al. 2020), have shown that the emission of P-bearing molecules arises from regions associated with shocks, and not from the central hot molecular core surrounding the newly formed protostars, which clearly rule out desorption due to heating.

4.2. Molecular ratios of P-bearing species: role of cosmic-rays and photochemistry

It is still not fully understood what the main carrier of P in the ISM is. The pioneering chemical models by Thorne et al. (1984) proposed PO as the most abundant P-bearing molecule in the ISM. However, subsequent studies by Millar et al. (1987) and Adams et al. (1990) indicated that PO is expected to have a lower abundance than that of PN in the ISM. More recently, the chemical models by Jiménez-Serra et al. (2018) proposed that PH$_3$ could be the main carrier of P on the surface of dust grains due to rapid hydrogenation of atomic P, and hence that it might be also relatively abundant in the gas phase if efficiently desorbed. In the last years, several observations of P-bearing species have allowed us to quantify the relative abundances of the different species, which are summarised in Table 3 (see references therein). In Galactic star-forming environments (low- and high-mass star-forming regions and protostellar shocks), the PO/PN ratio found is usually >1, with values up to ∼6 (Table 3). In molecular clouds of the CMZ of our Galaxy, the only detection of PO provides PO/PN ratio of 1.5 ± 0.4 (Table 3). In the GMCs 4 and 6 of NGC 253 we found that the PO/PN ratio is <1.7 and <1.3, respectively.

Rivilla et al. (2020) found in the AFGL 5142 star-forming region that the PO/PN ratios in different shocked regions decrease with decreasing distance to the source of ultraviolet (UV) photons (the central protostar). These authors suggested that the abundance of P-bearing molecules could be regulated by the photo-destruction if PO is more efficiently photo-destroyed than PN, as proposed by Jiménez-Serra et al. (2018). This might

Table 3. PO/PN ratios in NGC 253 and several regions in our Galaxy.

Source	[PO/PN]	[PH$_3$/PN]	Region type
Extragalactic			
NGC 253 – GMC 4	<1.7	<5.2	EGMC
NGC 253 – GMC 6	<1.3	<2.7	EGMC
Galactic Centre			
G+0.693−0.027 [1]	1.5±0.4	−	GCMC
S+0.24+0.01 [1]	<2.7	−	GCMC
M−0.02−0.07 [1]	<3.1	−	GCMC
SgrB2 N [1]	<1.8	−	MSFR
	<3.2	−	
SgrB2 M [1]	<6.8	−	MSFR
	<3.5	−	
Galactic disk star-forming regions			
AFGL5142 P1 [2]	<1.1	−	MSFR
AFGL5142 P2 [2]	0.6 ± 0.2 / 1.8	−	MSFR
AFGL5142 P3 [2]	1.4 ± 0.3 / 3.3	−	MSFR
AFGL5142 P4 [2]	1.6 ± 0.2 / 4.4	−	MSFR
AFGL5142 P5 [2]	2.6 ± 0.6 / 6.4	−	MSFR
AFGL5142 P6 [2]	2.2 ± 0.6 / 4.6	−	MSFR
W5 1 [3]	1.9	−	MSFR
W3(OH) [3]	3	−	MSFR
Orion plateau [4]	2.7	−	MSFR
L1157-B1 [5]	2.6	<1.1	LMSFR
			(protostellar shock)
B1-a [6]	1-3	−	LMSFR

Notes. Region types are as follows: Extragalactic giant molecular clouds (EGMC), Galactic Centre molecular clouds (GCMC), massive star-forming regions (MSFR), and low-mass star-forming regions (LMSFR). [1]Rivilla et al. (2018). [2]Different spots with PN and PO emission identified towards the massive star-forming region AFGL 5142 by Rivilla et al. (2020). Two different values are presented: those derived from an LTE analysis (left), and those derived from a non-LTE analysis assuming T_{kin} = 20 K and gas density of 10^5 cm^{-3}. [3]Rivilla et al. (2016), [4]Bernal et al. (2021), [5]Lefloch et al. (2016), [6]Bergner et al. (2019).

explain why the searches of PO towards the CMZ of NGC 253 and our Galaxy resulted in non-detections, with the only exception of the molecular cloud G+0.693−0.027 (Rivilla et al. 2018). The CMZ of galaxies harbor high cosmic-ray ionisation rates (ζ). Goto et al. (2014) found that ζ is well above 10^{-15} s^{-1} in the centre of our Galaxy, several orders of magnitude higher than the standard Galactic value of $\zeta \sim 1.3 \times 10^{-17}$ s^{-1} (e.g. Padovani et al. 2009). In the CMZ of NGC 253, although the values of ζ are not well constrained yet, recent ALCHEMI-based research has shown that they are between 10^{-11} and 10^{-14} s^{-1} (Holdship et al. 2021; Harada et al. 2021). This high ζ produces a field of secondary ultraviolet (UV) photons, which might result in the aforementioned more efficient photo-destruction of PO than PN. If this is the case, the abundance of PO would significantly decrease in galactic CMZs, producing values of PO/PN < 1.

In any case, we note that the upper limits derived for the PO abundance towards the CMZ of NGC 253 and other regions in the CMZ of our Galaxy (Table 3) do not allow us to firmly confirm that the ratio PO/PN < 1. Deeper observations, both in the Galactic disk and towards more molecular clouds in the CMZ of our Galaxy and other galaxies, are needed to confirm this hypothesis.

Regarding PH$_3$, we found that PH$_3$/PN is <5.2 and <2.7 in GMCs 4 and 6, respectively. These upper limits indicate that PH$_3$ is not significantly more abundant than PN in the gas phase, con-

firming the previous result by Lefloch et al. (2016), who found that PH$_3$/PN < 1.1 in a Galactic protostellar shock (Table 3). As for the case of PO, deeper observations will be needed to confirm whether PH$_3$ are equally or less abundant than PN in NGC 253.

4.3. Comparison with chemical models

Based on the observational evidence, we have discussed in the Sects. 4.1 and 4.2 the possible role of shocks and cosmic rays (+ photochemistry) shaping the molecular abundances of P-bearing species in the ISM. In this section, we compare the observational results with the predictions of the chemical models presented by Jiménez-Serra et al. (2018), who studied the chemistry of P-bearing molecules under different physical conditions such as presence of shocks, and different cosmic-ray ionisation rates (ζ) and gas densities.

The shock models predict high gas-phase abundances of P-bearing species, which are significantly enhanced due to grain sputtering. For PN, its abundance is $(1-5) \times 10^{-10}$, which is more than one order of magnitude higher than the abundances we derived towards the GMCs of NGC 253 of $(0.4-0.8) \times 10^{-11}$ (assuming that PN and dust trace similar gas). Therefore, the models based solely on shocks fail to explain the relatively low PN abundances observed in NGC 253, and hence an additional agent is needed.

As discussed in Sect. 4.2, cosmic rays can also strongly affect the chemistry of P-bearing molecules. The secondary UV-photon radiation field induced by an enhancement of ζ can also partially photodissociate the P-bearing molecules. This will regulate the PO/PN ratio (Sect. 4.2), but will also decrease the overall molecular abundances. When Jiménez-Serra et al. (2018) introduced a high cosmic-ray ionisation rates of $\zeta = 10^{-13}$ s^{-1} in the shock models with pre-shock densities of $n(H) = 2 \times 10^4$ cm^{-3} (see their Fig. 8), the predicted PN abundances decrease by one order of magnitude at the post-shock stage, reaching several 10^{-11}, which is more similar to the ones we derived for NGC 253. Moreover, we note that these models predict a PO/PN ratio <1, which is consistent with the upper limits found in the CMZs of NGC 253. These values for ζ and gas density match well with the expected physical properties of the GMCs in the CMZ of NGC 253. As mentioned in Sect. 4.2, recent ALCHEMI works indicate that ζ is $10^{-11}-10^{-14}$ s^{-1} (Holdship et al. 2021; Harada et al. 2021), while the non-LTE analysis of PN (Sect. 3.2) shows that the most likely gas density is around $n(H_2) = 3\times10^4$ cm^{-3}, and thus[7] $n(H) = 6\times10^4$ cm^{-3}.

5. Conclusions

We searched for P-bearing molecules in the Central Molecular Zone of the starburst Galaxy NGC 253 using the unbiased ALCHEMI spectral survey. Phosphorus nitride (PN) was detected towards two of the Giant Molecular clouds (GMCs 4 and 6) in NGC 253, being the first detections of a P-bearing molecule in an extragalactic environment. An LTE analysis yields total PN beam-averaged column densities of $N = (1.20 \pm 0.09) \times 10^{13}$ cm^{-2} and $N = (6.5 \pm 1.6) \times 10^{12}$ cm^{-2} for GMCs 6 and 4, respectively, and an excitation temperature of $T_{ex} = (4.4 \pm 1.3)$ K towards GMC 6. The derived molecular abundances with respect to H$_2$ are $\chi = (8.0 \pm 1.0) \times 10^{-12}$ and

---

[7] We note that the non-LTE analysis uses the gas density of molecular hydrogen, $n(H_2)$, while the chemical models use the gas density of atomic hydrogen, $n(H)$. Assuming a molecular cloud in which all the hydrogen is in molecular form, $n(H) = 2\times n(H_2)$.

$\chi = (4.4 \pm 1.2) \times 10^{-12}$ for GMCs 6 and 4, respectively. A non-LTE analysis derives a column density consistent with the LTE values, and confirms that the PN transitions are sub-thermally excited in a gas with volume density of the order of 10^4 cm^{-3}. Other P-bearing molecules like PO, PH$_3$, CP, and CCP were not detected. We provide upper limits for their column densities in GMCs 4 and 6. The derived PO/PN ratios are <1.3 and <1.7 for GMCs 4 and 6, respectively.

The comparison between the current observational evidence of P-bearing molecules in Galactic and extragalactic environments and the available chemical models indicates that the chemistry of P-bearing species is mainly regulated by shocks, which contribute to desorb the P-content locked on the dust via grain sputtering, and subsequent gas-phase photochemistry that can regulate the molecular abundances of P-bearing species and the PO/PN ratio. This photochemistry can be triggered by the presence of an intense cosmic-ray flux, as expected in the CMZ of galaxies, or by a nearby protostar in star-forming regions.

References

Adams, N. G., McIntosh, B. J., & Smith, D. 1990, A&A, 232, 443
Agúndez, M., Cernicharo, J., & Guélin, M. 2007, ApJ, 662, L91
Agúndez, M., Cernicharo, J., Decin, L., Encrenaz, P., & Teyssier, D. 2014, ApJ, 790, L27
Aladro, R., Martín, S., Riquelme, D., et al. 2015, A&A, 579, A101
Ando, R., Nakanishi, K., Kohno, K., et al. 2017, ApJ, 849, 81
Asplund, M., Grevesse, N., Sauval, A. J., & Scott, P. 2009, ARA&A, 47, 481
Ba, Y.-A., Dubernet, M.-L., Moreau, N., & Zwölf, C. M. 2020, Atoms, 8, 69
Bailleux, S., Bogey, M., Demuynck, C., Liu, Y., & Walters, A. 2002, J. Mol. Spectr., 216, 465
Bendo, G. J., Beswick, R. J., D'Cruze, M. J., et al. 2015, MNRAS, 450, L80
Bergner, J. B., Öberg, K. I., Walker, S., et al. 2019, ApJ, 884, L36
Bernal, J. J., Koelemay, L. A., & Ziurys, L. M. 2021, ApJ, 906, 55
Bregman, J. D., Lester, D. F., & Rank, D. M. 1975, ApJ, 202, L55
Cazzoli, G., Cludi, L., & Puzzarini, C. 2006, J. Mol. Struct., 780, 260
Dubernet, M. L., Alexander, M. H., Ba, Y. A., et al. 2013, A&A, 553, A50
Endres, C. P., Schlemmer, S., Schilke, P., Stutzki, J., & Müller, H. S. P. 2016, J. Mol. Spectr., 327, 95

Fontani, F., Rivilla, V. M., Caselli, P., Vasyunin, A., & Palau, A. 2016, ApJ, 822, L30
Fontani, F., Rivilla, V. M., van der Tak, F. F. S., et al. 2019, MNRAS, 489, 4530
Foreman-Mackey, D., Hogg, D. W., Lang, D., & Goodman, J. 2013, PASP, 125, 306
Friedman, S. D., Howk, J. C., Andersson, B. G., et al. 2000, ApJ, 538, L39
Goto, M., Geballe, T. R., Indriolo, N., et al. 2014, ApJ, 786, 96
Halfen, D. T., Clouthier, D. J., & Ziurys, L. M. 2008, ApJ, 677, L101
Harada, N., Martín, S., Mangum, J. G., et al. 2021, ApJ, 923, 24
Hoeft, J., Tiemann, E., & Törring, T. 1972, Z. Naturforsch. Teil A, 27, 703
Holdship, J., Viti, S., Martín, S., et al. 2021, A&A, 654, A55
Jiménez-Serra, I., Viti, S., Quénard, D., & Holdship, J. 2018, ApJ, 862, 128
Kanata, H., Yamamoto, S., & Saito, S. 1988, J. Mol. Spectr., 131, 89
Koo, B.-C., Lee, Y.-H., Moon, D.-S., Yoon, S.-C., & Raymond, J. C. 2013, Science, 342, 1346
Larson, H. P., Treffers, R. R., & Fink, U. 1977, ApJ, 211, 972
Lefloch, B., Vastel, C., Viti, S., et al. 2016, MNRAS, 462, 3937
Leroy, A. K., Bolatto, A. D., Ostriker, E. C., et al. 2015, ApJ, 801, 25
Levenberg, K. 1944, Q. Appl. Math., 2, 164
Maciá, E. 2019, The Chemical Evolution of Phosphorus An Interdisciplinary Approach to Astrobiology (New Jersey: Apple Academic Press)
Mangum, J. G., Darling, J., Henkel, C., et al. 2013, ApJ, 779, 33
Mangum, J. G., Ginsburg, A. G., Henkel, C., et al. 2019, ApJ, 871, 170
Marble, A. R., Engelbracht, C. W., van Zee, L., et al. 2010, ApJ, 715, 506
Marquardt, D. W. 1963, J. Soc. Ind. Appl. Math., 11, 431
Martín, S., Mauersberger, R., Martín-Pintado, J., Henkel, C., & García-Burillo, S. 2006, ApJS, 164, 450
Martín, S., Martín-Pintado, J., & Mauersberger, R. 2009, ApJ, 694, 610
Martín, S., Martín-Pintado, J., Blanco-Sánchez, C., et al. 2019, A&A, 631, A159
Martín, S., Mangum, J. G., Harada, N., et al. 2021, A&A, 656, A46
Meier, D. S., Walter, F., Bolatto, A. D., et al. 2015, ApJ, 801, 63
Milam, S. N., Halfen, D. T., Tenenbaum, E. D., et al. 2008, ApJ, 684, 618
Millar, T. J., Bennett, A., & Herbst, E. 1987, MNRAS, 229, 41P
Mills, E. A. C., Gorski, M., Emig, K. L., et al. 2021, ApJ, 919, 105
Mininni, C., Fontani, F., Rivilla, V. M., et al. 2018, MNRAS, 476, L39
Molaro, P., Levshakov, S. A., D'Odorico, S., Bonifacio, P., & Centurión, M. 2001, ApJ, 549, 90
Müller, H. S. P. 2013, J. Quant. Spectr. Rad. Transf., 130, 335
Müller, H. S. P., Thorwirth, S., Roth, D. A., & Winnewisser, G. 2001, A&A, 370, L49
Müller-Sánchez, F., González-Martín, O., Fernández-Ontiveros, J. A., Acosta-Pulido, J. A., & Prieto, M. A. 2010, ApJ, 716, 1166
Najar, F., Naouai, M., Hanini, H. E., & Jaidane, N. 2017, MNRAS, 472, 2919
Padovani, M., Galli, D., & Glassgold, A. E. 2009, A&A, 501, 619
Rekola, R., Richer, M. G., McCall, M. L., et al. 2005, MNRAS, 361, 330
Requena-Torres, M. A., Martín-Pintado, J., Rodríguez-Franco, A., et al. 2006, A&A, 455, 971
Rivilla, V. M., Fontani, F., Beltrán, M. T., et al. 2016, ApJ, 826, 161
Rivilla, V. M., Jiménez-Serra, I., Zeng, S., et al. 2018, MNRAS, 475, L30
Rivilla, V. M., Drozdovskaya, M. N., Altwegg, K., et al. 2020, MNRAS, 492, 1180
Robitaille, T. P., & Whitney, B. A. 2010, ApJ, 710, L11
Tenenbaum, E. D., Woolf, N. J., & Ziurys, L. M. 2007, ApJ, 666, L29
Thorne, L. R., Anicich, V. G., Prasad, S. S., & Huntress, W. T. Jr. 1984, ApJ, 280, 139
Turner, B. E., & Bally, J. 1987, ApJ, 321, L75
Ulvestad, J. S., & Antonucci, R. R. J. 1997, ApJ, 488, 621
van der Tak, F. F. S., Black, J. H., Schöier, F. L., Jansen, D. J., & van Dishoeck, E. F. 2007, A&A, 468, 627
Yamaguchi, T., Takano, S., Sakai, N., et al. 2011, PASJ, 63, L37
Ziurys, L. M. 1987, ApJ, 321, L81
Ziurys, L. M., Schmidt, D. R., & Bernal, J. J. 2018, ApJ, 856, 169

Appendix A: Additional molecular line analysis towards NGC 253 GMCs

Figures A.1 and A.2 show the spectra and the LTE fits of ^{29}SiO and C^{34}S analysed towards the GMCs 4 and 6, respectively. Figures A.3 to A.9 show the spectra, LTE fits, and upper limits of PN, ^{29}SiO, and C^{34}S analysed towards the rest of the GMCs. Table A.1 lists the physical parameters of the emission of PN, ^{29}SiO, and C^{34}S towards the GMCs with no PN detection, obtained from the LTE analysis.
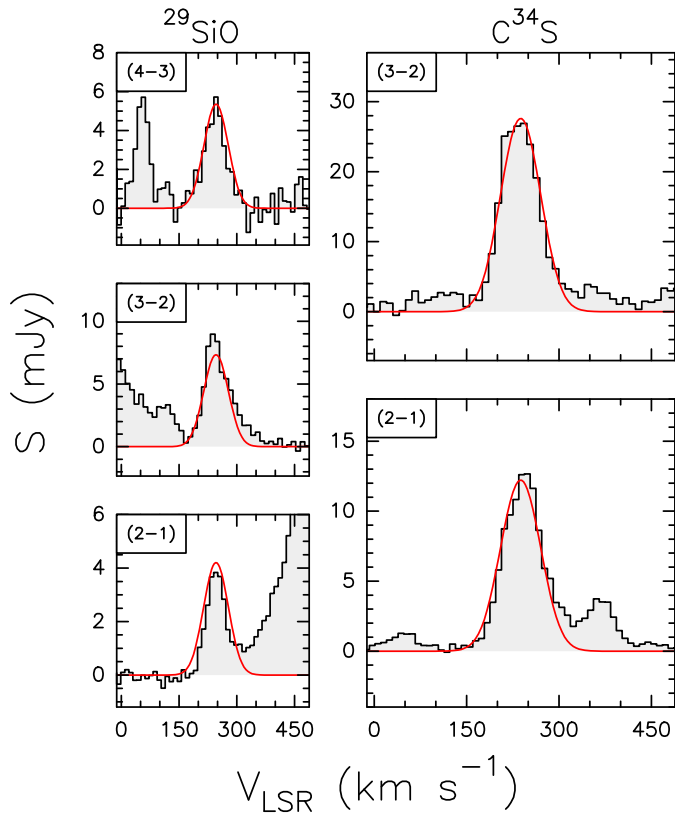
Fig. A.1. Spectra of ^{29}SiO and C^{34}S towards GMC 4 are shown with grey histograms. The transition is indicated in the upper left of each panel. The red lines indicate the LTE best fits.
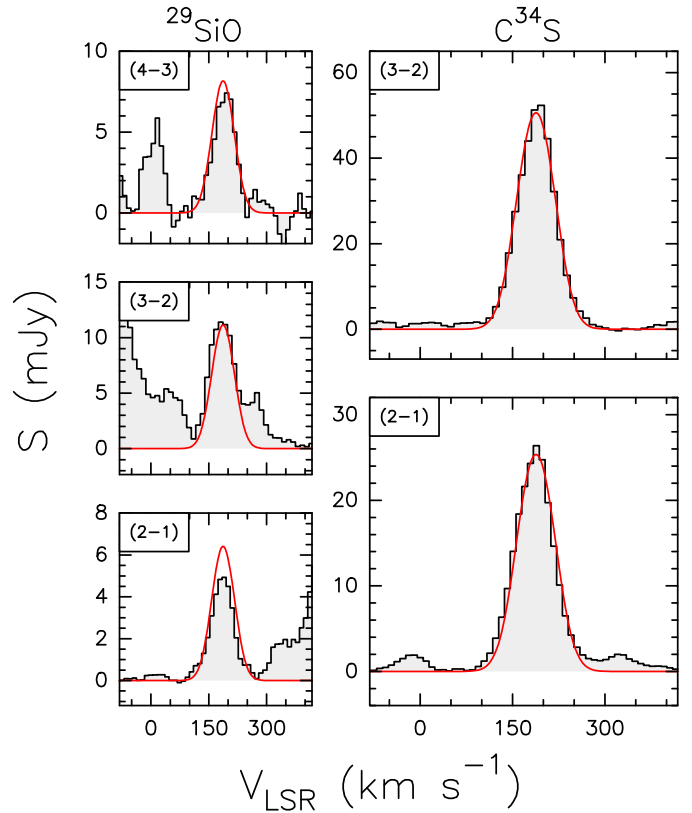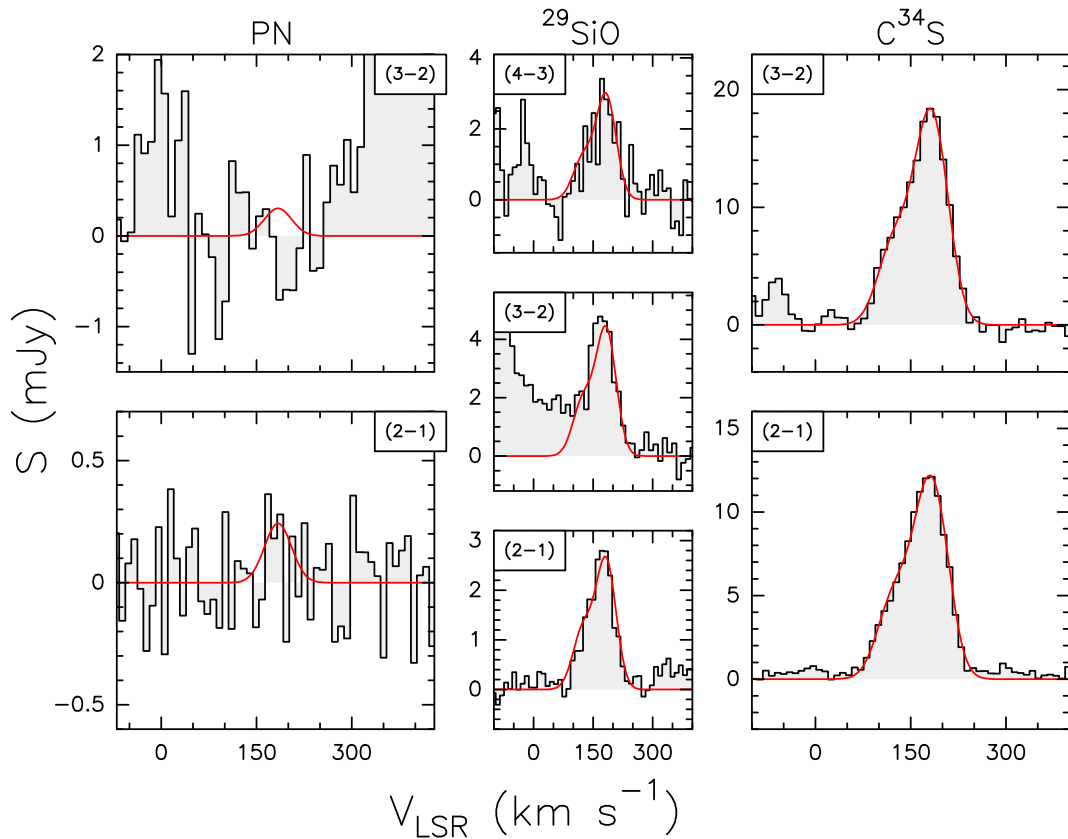

Fig. A.2. Spectra of ^{29}SiO and C^{34}S towards GMC 6 are shown with grey histograms. The transition is indicated in the upper left of each panel. The red lines indicate the LTE best fits.
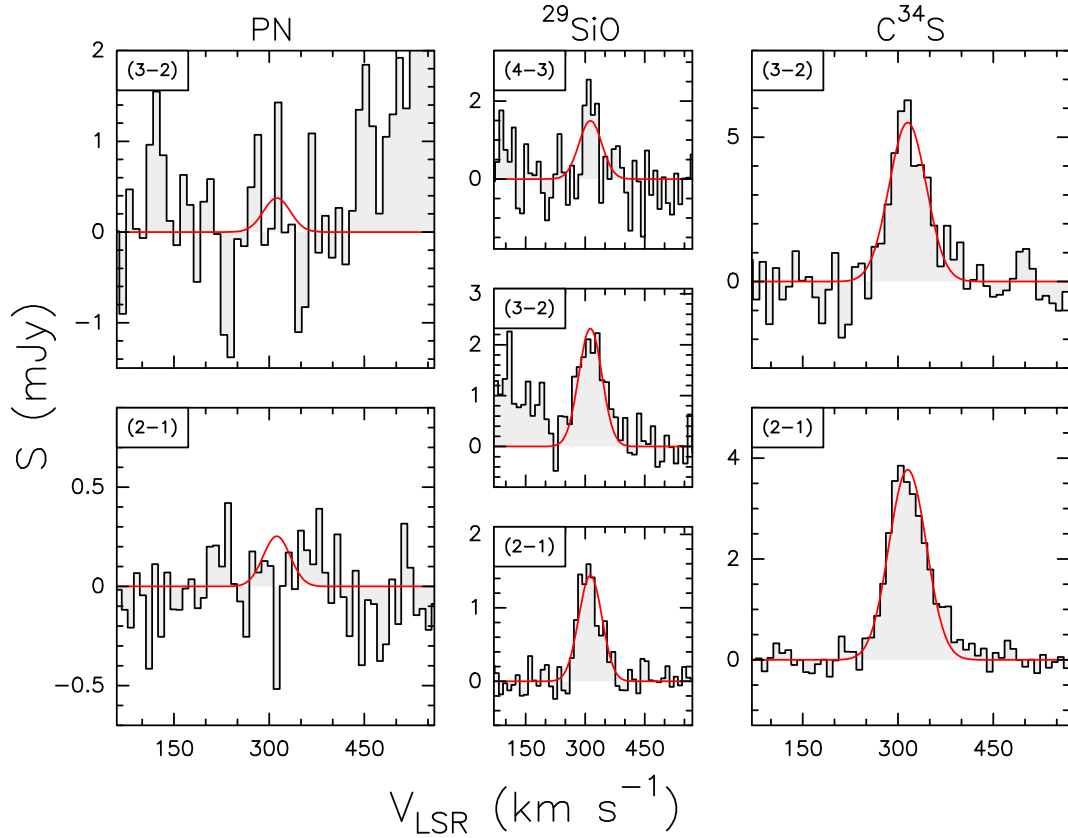
Fig. A.3. Spectra of PN, ^{29}SiO, and C^{34}S towards GMC 1 are shown with grey histograms. The transition is indicated in the upper left of each panel. The red lines indicate the LTE best fits except for PN, for which the red line indicates an upper limit.
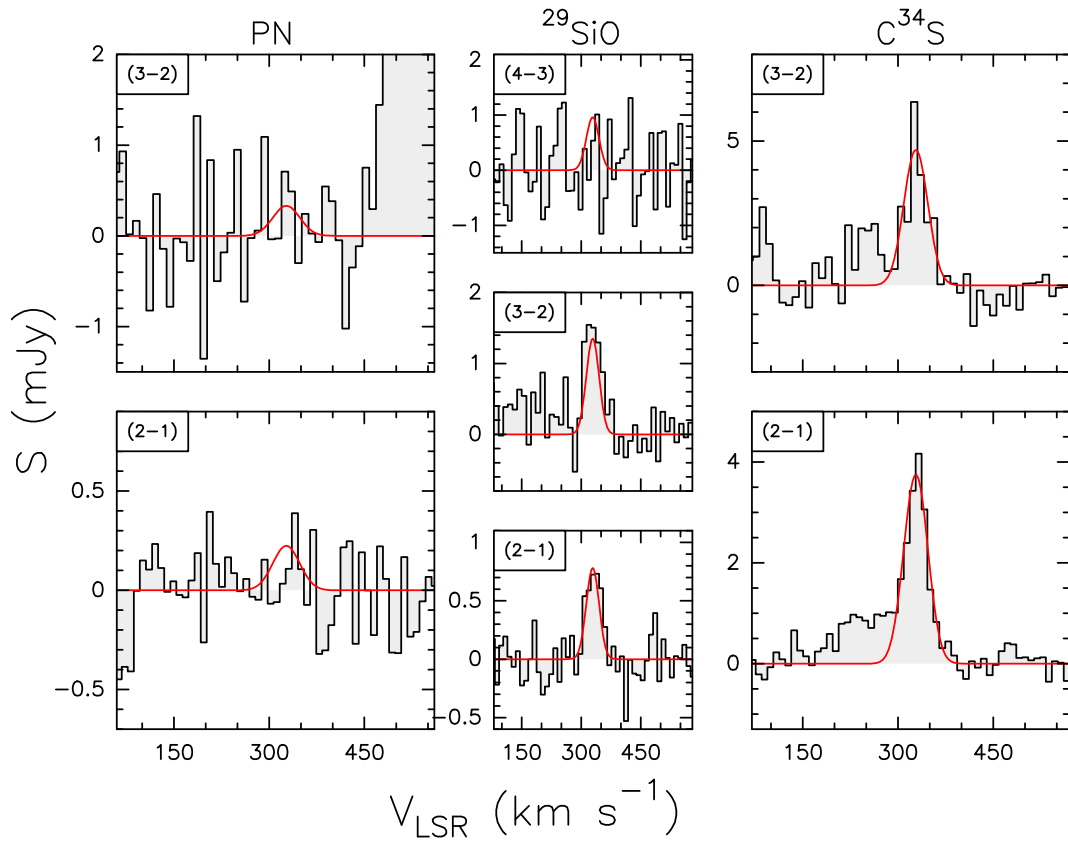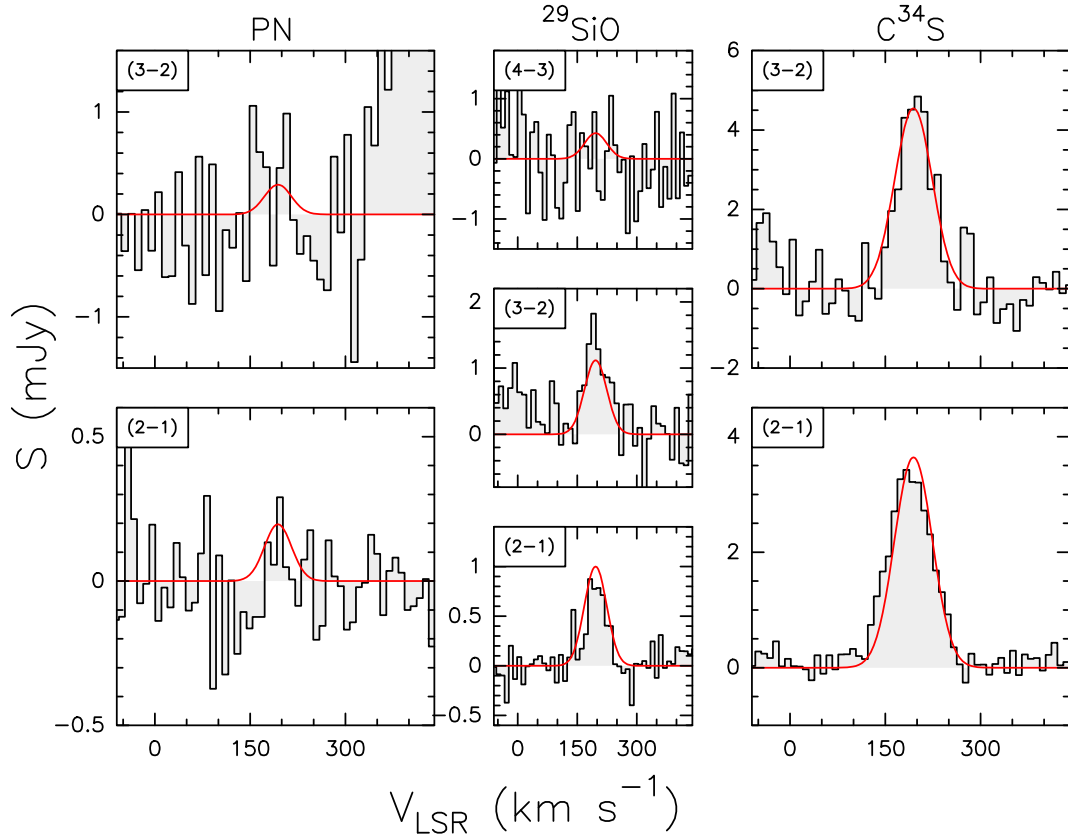
Fig. A.4. Spectra of PN, ^{29}SiO, and C^{34}S towards GMC 2 are shown with grey histograms. The transition is indicated in the upper left of each panel. The red lines indicate the LTE best fits except for PN, for which the red line indicates an upper limit.
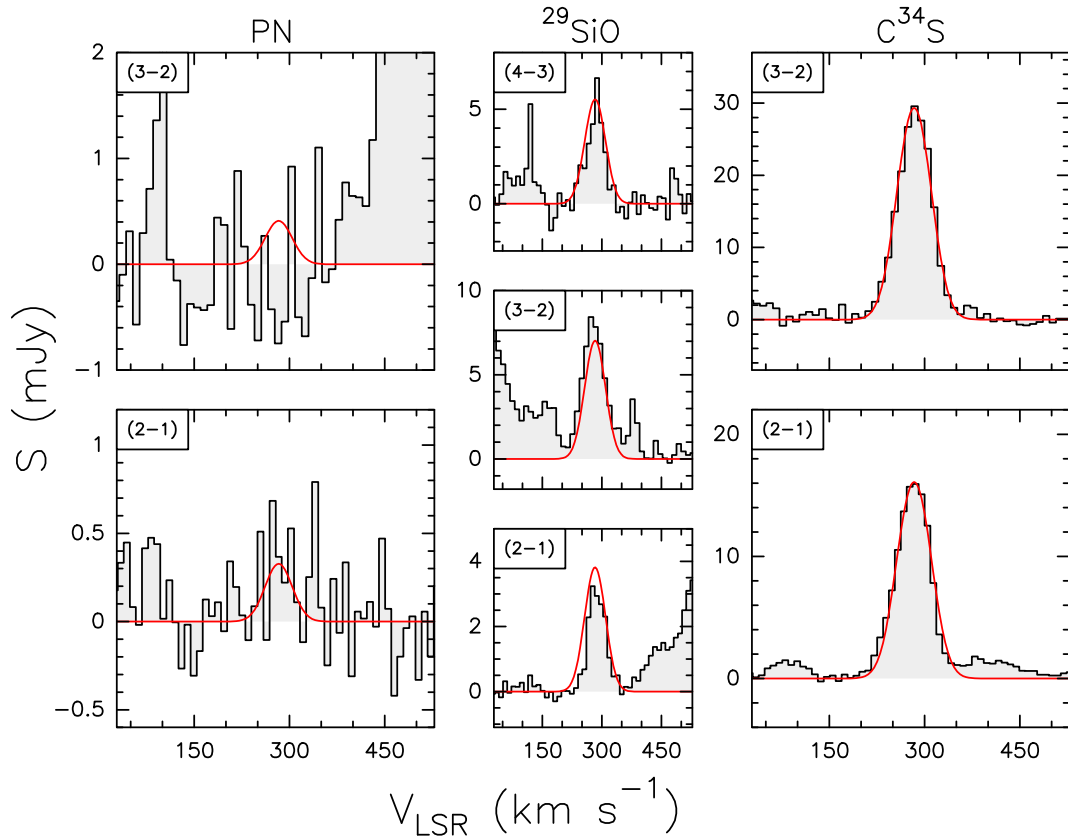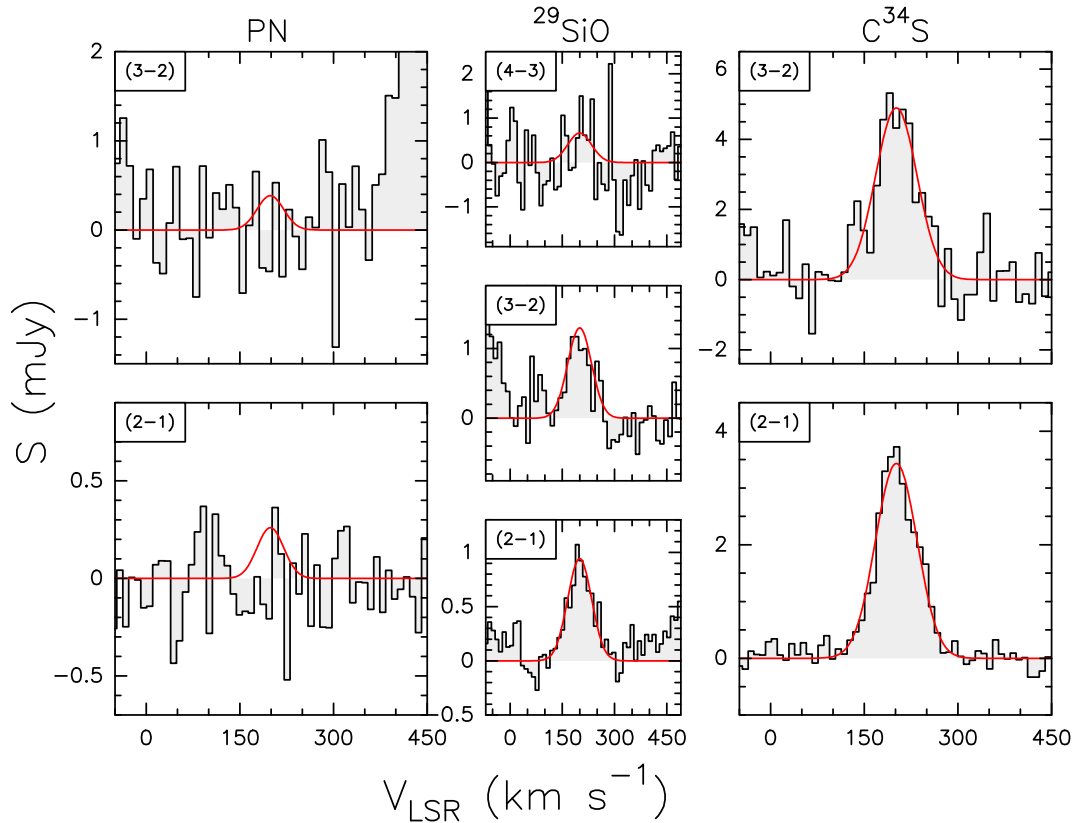
Fig. A.5. Spectra of PN, ^{29}SiO, and C^{34}S towards GMC 3 are shown with grey histograms. The transition is indicated in the upper left of each panel. The red lines indicate the LTE best fits except for PN, for which the red line indicates an upper limit.
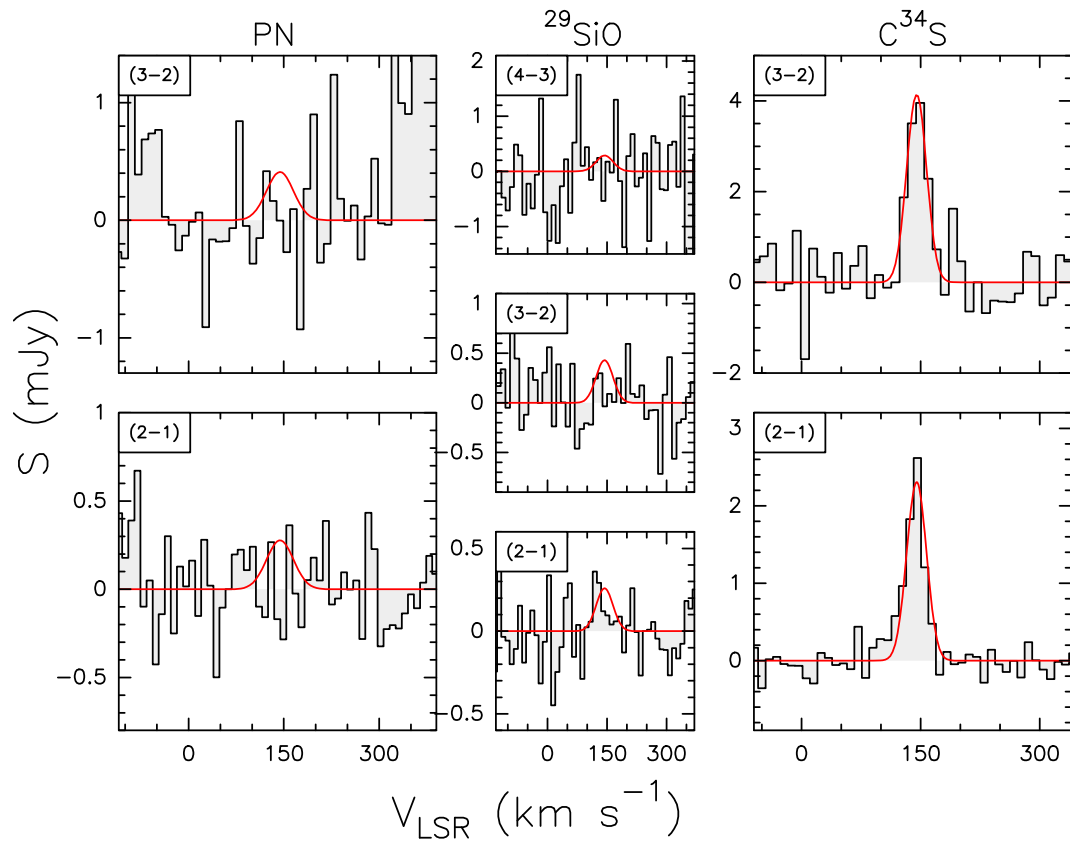

Fig. A.6. Spectra of PN, ^{29}SiO, and C^{34}S towards GMC 7 are shown with grey histograms. The transition is indicated in the upper left of each panel. The red lines indicate the LTE best fits except for PN, for which the red line indicates an upper limit.

Fig. A.7. Spectra of PN, ^{29}SiO, and C^{34}S towards GMC 8 are shown with grey histograms. The transition is indicated in the upper left of each panel. The red lines indicate the LTE best fits except for PN, for which the red line indicates an upper limit.

Fig. A.8. Spectra of PN, ^{29}SiO, and C^{34}S towards GMC 9 are shown with grey histograms. The transition is indicated in the upper left of each panel. The red lines indicate the LTE best fits, except for PN, for which the red line indicates an upper limit.

Fig. A.9. Spectra of PN, ^{29}SiO, and C^{34}S towards GMC 10 are shown with grey histograms. The transition is indicated in the upper left of each panel. The red lines indicate the LTE best fit for C^{34}S, while for ^{29}SiO and PN the red line indicates an upper limit.

Table A.1. Physical parameters of the emission of PN, ^{29}SiO, and C^{34}S towards the GMCs 1, 2, 3, 7, 8, 9, and 10 obtained from the LTE analysis.

Molecule	N (cm^{-2}) $\times 10^{13}$	T_{ex} (K)	v_{LSR} (km s^{-1})	FWHM (km s^{-1})
		GMC 1		
PN	<0.24	4.4[a]	315[a]	50[a]
^{29}SiO	2.0±0.5	4.9±0.4	313±3	68±8
C^{34}S	9.2±1.5	5.0±0.4	315.4±1.7	68±4
		GMC 2		
PN	<0.21	4.4[a]	328[a]	50[a]
^{29}SiO	0.56±0.11	5[a]	329±4	38±9
C^{34}S	7±3	4.4±0.6	328.2±2.2	44±5
		GMC 3		
PN	<0.4	4.4[a]	283[a]	50[a]
^{29}SiO	4.3±0.6	5.5±0.3	283.2±1.9	60±4
C^{34}S	32.8±1.3	6.11±0.16	283.6±0.4	60.3±1.0
		GMC 7		
PN	<0.3	4.4[a]	184[a]	50[a]
	5.8±0.9	5.6±0.4	125.2[a]	60.2[a]
^{29}SiO[b]	3.0±0.4	5.0±0.3	183.0[a]	58.3[a]
	1.5±0.5	4.7±0.6	125.2[a]	60.2[a]
C^{34}S[b]	27.4±2.3	5.08±0.08	183.0±1.6	58.3±2.0
	11.5±1.9	4.88±0.17	125.2±4.1	60.2±5.3
		GMC 8		
PN	<0.19	4.4[a]	195[a]	50[a]
^{29}SiO	2.5±1.7	3.6±0.5	197±6	65±13
C^{34}S	7±3	4.4±0.6	194.6±1.7	68±4
		GMC 9		
PN	<0.3	4.4[a]	200[a]	50[a]
^{29}SiO	1.9±0.8	4.2±0.6	200±7	80±15
C^{34}S	9.7±1.5	4.9±0.3	201.5±1.8	77±4
		GMC 10		
PN	<0.3	4.4[a]	145[a]	50[a]
^{29}SiO	<0.3	5[a]	145[a]	50[a]
C^{34}S	2.0±0.5	6.2±0.9	145.1±1.1	29±3

[a] Parameter fixed. [b] Two velocity components were used in the analysis.